Robust Hyperspectral Anomaly Detection via Bootstrap Sampling-based Subspace Modeling in the Signed Cumulative Distribution Transform Domain

Abu Hasnat Mohammad Rubaiyat
Amentum
Hanover, MD 21076
abuhasnatmohammad.rubaiyat@us.amentum.com

Jordan Vincent
Tekla Research
Fredericksburg, VA 22407
jordan.e.vincent2.ctr@us.navy.mil

Colin Olson
U.S. Naval Research Laboratory
Washington, DC 20375
colin.c.olson.civ@us.navy.mil

Abstract

This paper introduces an approach that combines a transport-based model of hyperspectral pixels and a bootstrap sampling strategy to construct an ensemble of background subspaces in the signed cumulative distribution transform (SCDT) domain for robust anomaly detection in hyperspectral images characterized by complex and varied background clutter. Each spectral signal (i.e., pixel) is treated as an observation of an unknown background template pattern that has undergone unknown, but restricted, deformation due to factors such as shadowing, look angle, or atmospheric absorption. When combined with the SCDT—a transport-based transform with close connections to one-dimensional Wasserstein embedding—the model induces convexity of hyperspectral pixel representations in the SCDT space and facilitates the construction of subspace models that characterize dominant background signals. A bootstrap sampling strategy in the ambient domain yields an ensemble of background subspace models in SCDT domain and anomalies are subsequently detected as pixels that do not conform to any of the learned subspace models. Experiments on six benchmark hyperspectral datasets demonstrate that the approach effectively captures spectral variability and reliably detects anomalies with low false alarm rates, outperforming state-of-the-art comparison methods in most cases. These results underscore the potential of transport-based subspace representations for robust and interpretable hyperspectral anomaly detection across diverse imaging scenarios. Finally, the geodesic properties of the SCDT embedding are leveraged to provide a geometric interpretation of the method via visualization of paths between test signals and their subspace projections.

1 Introduction

Hyperspectral imaging (HSI) captures detailed spectral information, enabling the detection of subtle differences between ground objects. Unlike standard RGB cameras, HSI sensors densely sample the spectrum, preserving fine material information that is often lost in conventional imaging. Hyperspectral anomaly detection (HAD) aims to identify pixels in an HSI whose spectral signatures deviate from the surrounding background. HAD has proven effective in numerous applications, including environmental monitoring Xu et al. [2019], intelligent agriculture Goel et al. [2003], mineral exploration Tan et al. [2019], and defense or surveillance Su et al. [2021]. However, the task

Proceedings of the 1st Conference on Topology, Algebra, and Geometry in Data Science(TAG-DS 2025).

remains challenging due to variability in background spectra, atmospheric conditions, illumination changes, and alterations in target properties. Unsupervised HAD methods are particularly useful in such scenarios, as they can reliably detect anomalies without requiring prior information about target or background signatures.

HAD methods can be grouped into model-based, representation-based, and deep learning-based approaches. Model-based techniques, such as Reed-Xiaoli (RX) Reed and Yu [1990] and its variants Nasrabadi [2008], Kwon and Nasrabadi [2005], Matteoli et al. [2010], detect anomalies by assuming specific statistical distributions for the background, but their performance may be limited when these assumptions do not fully hold. Representation-based methods overcome this limitation by reconstructing background pixels from a dictionary and identifying anomalies as deviations Liu et al. [2012], Xu et al. [2015], though they are often iterative and require careful parameter tuning. Deep learning approaches, including autoencoders and self-supervised models Fan et al. [2021], Wang et al. [2023b,a], offer strong detection performance but lack explicit background modeling, which can limit interpretability and theoretical guarantees Li et al. [2023].

Optimal transport–based techniques have recently been applied to estimation and detection problems due to their ability to simplify certain nonlinear tasks Park et al. [2018], Aldroubi et al. [2022], Thareja et al. [2022], Rubaiyat et al. [2022]. In Emerson et al. [2018], a kernel principal component analysis (kPCA)–based background modeling approach for HSI was proposed, utilizing an optimal transport geodesic–based augmentation strategy to enhance the kPCA feature space. Following this line of research, Rubaiyat et al. [2025] introduced an optimal transport–based anomaly detection method that combines the SCDT with principal component analysis (PCA) to construct a linear subspace for modeling the HSI background in the transform domain. Anomalies were identified as signals that did not conform to this subspace. While effective, this single-subspace assumption may not adequately capture the variability present in many real hyperspectral scenes. The method we propose here extends this framework by constructing multiple subspaces in the SCDT domain, facilitating a more accurate representation of the spectral diversity in hyperspectral data.

We briefly discuss the application of the SCDT to HAD in Section 2, and in Sections 3.1 and 3.2 we present a transport-based mathematical model to represent hyperspectral pixels, assuming that their spectral signals are generated from a set of templates under unknown deformations. In Section 3.3 we use a bootstrap sampling strategy in the ambient domain to construct multiple subspaces in the SCDT domain from the sampled signals. Anomalies are then identified as pixels whose spectral signatures do not conform to any of the constructed subspaces, indicating deviations from the proposed transport model. In Section 3.4 we leverage the geodesic properties of the SCDT embedding to provide a geometric interpretation of the HAD method by visualizing the paths between test signals and their projections onto the constructed subspaces. We evaluate the approach on multiple hyperspectral datasets and compare against competing methods in Section 4 before concluding in Section 5.

2 Background on Hyperspectral Anomaly Detection in SCDT Domain

2.1 Signed Cumulative Distribution Transform

Park et al. [2018] first introduced the cumulative distribution transform (CDT), a transport-based transform, for positive probability densities. Consider a signal $s(x)$ and a fixed reference $s_0(y)$, both positive within their respective domains Ω_s and Ω_{s_0}, with unit total mass: $\int_{\Omega_s} s(u)du = \int_{\Omega_{s_0}} s_0(u)du = 1$. The CDT of s with respect to reference s_0 is defined as $s^*(y) = S^{-1}(S_0(y))$, where $S(x) = \int_{\inf(\Omega_s)}^{x} s(u)du$ and $S_0(y) = \int_{\inf(\Omega_{s_0})}^{y} s_0(u)du$. When the reference signal s_0 is uniform, the CDT simplifies to:

$$s^*(y) = S^{-1}(y), \tag{1}$$

which is the formulation adopted throughout this work. Aldroubi et al. [2022] extended the CDT framework to handle general finite signed signals, introducing the signed cumulative distribution transform (SCDT). For a non-negative signal $s(x)$ with arbitrary total mass, the SCDT is given by:

$$\widehat{s}(y) = \begin{cases} (s^*(y), \|s\|_{L_1}), & \text{if } s \neq 0 \\ (0, 0), & \text{if } s = 0, \end{cases} \tag{2}$$

where s^* represents the CDT (eq. (1)) of the normalized signal $\frac{s}{\|s\|_{L_1}}$. For a general signed signal $s(x)$, the transform first decomposes s into: $s(x) = s^+(x) - s^-(x)$, where $s^+(x)$ and $s^-(x)$ are the

absolute values of the positive and negative components of the signal $s(x)$. The SCDT of $s(x)$ is then expressed as:

$$\widehat{s}(y) = \left(\widehat{s}^{+}(y), \widehat{s}^{-}(y)\right), \tag{3}$$

where $\widehat{s}^{+}(y)$ and $\widehat{s}^{-}(y)$ represent the transforms of the positive and negative components of $s(x)$, as defined in eq. (2).

2.2 SCDT Subspace Model for Hyperspectral Anomaly Detection

The SCDT possesses several useful properties, including composition and convexity properties Aldroubi et al. [2022], that help simplify data geometry Li et al. [2022], thereby making it more suitable for solving many nonlinear estimation and detection problems Rubaiyat et al. [2024a,b]. Rubaiyat et al. [2025] recently introduced an HAD method that leverages the SCDT in combination with subspace modeling of hyperspectral pixel signatures. In their framework, the spectral responses of the background (non-anomalous) pixels are assumed to follow a certain mathematical model:

$$\mathbb{S}^{(b)} = \left\{ s_j^{(b)} | s_j^{(b)} = g_j' \varphi^{(b)} \circ g_j, g_j \in \mathcal{G} \right\}, \tag{4}$$

where each spectral signal $s_j^{(b)}$ is expressed as a deformed version of a template $\varphi^{(b)}$, and $\mathcal{G}$ represents a set of differentiable, increasing deformations, such as scaling or warping. Here, $s \circ g = s(g(x))$ denotes the composition of $s(x)$ with an invertible function $g(x)$, where $g' = dg(x)/dx$. For instance, under translation and scaling, $g(x) = \omega x - \mu$, yielding $s_g(x) = \omega s(\omega x - \mu)$. In the SCDT domain, these background spectra are assumed to be well approximated by a low-dimensional subspace, denoted as $\widehat{\mathbb{V}}^{(b)} = \text{Span}\left(\widehat{\mathbb{S}}^{(b)}\right)$. The anomaly score for a given test signal s is then computed as the distance between $\widehat{s}$ and its nearest point in $\widehat{\mathbb{V}}^{(b)}$; larger distances are expected for anomalous pixels compared to background pixels. While this approach performs well across various HSI datasets, the assumption in eq. (4)—that the hyperspectral scene is predominantly homogeneous—may not hold in more complex environments. In the following section, we extend this framework and propose an improved model to better represent background pixels.

3 Proposed Approach

This section presents a transport-based mathematical model for hyperspectral pixels, defines the HAD problem based on the model, and introduces a new method to address anomaly detection. Finally, it provides a geometric interpretation of the proposed approach.

3.1 Transport-based Model for Anomaly Detection Problem

Consider a hyperspectral image, $\mathbf{S} = \{s_i\}_{i=1}^{N} \in \mathbb{R}^{D \times N}$, where N denotes the total number of pixels and D is the number of spectral bands, with each spectral signal $s_i \in \mathbb{R}^{D}$. The pixels in $\mathbf{S}$ can be categorized into two groups: background (non-anomalous) and anomalous. In a homogeneous HSI setting, background pixels typically exhibit strong spectral correlation. Based on this assumption, the method proposed in Rubaiyat et al. [2025] modeled the spectral signatures of background pixels using a single representative set, as shown in eq. (4). However, in real-world scenarios, the background of an HSI usually comprises diverse materials and objects, such as vegetation, roads, buildings, and shadows. As a result, the model in eq. (4) is insufficient to fully represent the complexity of real HSI backgrounds. To address this, we model background signals as originating from a collection of templates, rather than a single template, with each spectral signal undergoing unknown deformations. Under this assumption, the set of all possible background signals is represented as a union of subsets, where each subset corresponds to the spectral signals generated from a specific template.

Let $\mathbb{S}^{(b)}$ denote the set of all possible background pixel responses. For a set of strictly increasing 1D deformations denoted as $\mathcal{G} \subset \mathcal{T}$, the 1D transport-based model for the set $\mathbb{S}^{(b)}$ is defined as:

$$\mathbb{S}^{(b)} = \bigcup_{m=1}^{M} \mathbb{S}_{\varphi_m^{(b)}, \mathcal{G}}, \text{ with } \mathbb{S}_{\varphi_m^{(b)}, \mathcal{G}} = \left\{ s_{j,m}^{(b)} | s_{j,m}^{(b)} = g_j' \varphi_m^{(b)} \circ g_j, g_j' > 0, g_j \in \mathcal{G} \right\}, \tag{5}$$

where $\mathcal{G}$ defined such that $\mathcal{G}^{-1} = \left\{\sum_{i=1}^{k} \alpha_i f_i, \;\; \alpha_i \geq 0\right\}$, $\{f_1, f_2, \ldots, f_k\}$ is a collection of linearly independent, strictly increasing functions over the signal domain, k is a positive integer, and $\mathcal{T}$ denotes the set of all increasing diffeomorphisms. In this formulation, the subset $\mathbb{S}_{\varphi_m^{(b)},\mathcal{G}}$ represents the spectral responses corresponding to the m-th background object and is generated from the template $\varphi_m^{(b)}$ under strictly increasing deformations specified by $\mathcal{G}$. In essence, each of the m background materials in a scene has an underlying template spectrum that undergoes deformations defined by $\mathcal{G}$. While these templates and deformations are unknown, the proposed approach uses the sampling scheme described below to construct subspaces that approximate the background subspaces corresponding to these theoretical ground truth templates, enabling effective anomaly detection.

Problem Statement: Let $\mathbf{S}$ denote a hyperspectral image (HSI) consisting of a large number of background pixels $\mathbf{S}^{(b)} \subseteq \mathbb{S}^{(b)}$ and a small number of anomalous pixels $\mathbf{S}^{(a)}$, with $\mathbf{S}^{(a)} \cap \mathbb{S}^{(b)} = \emptyset$. Suppose the background set $\mathbb{S}^{(b)}$ is characterized by the model in eq. (5). The objective is to decide, for a given pixel $s \in \mathbf{S}$, whether it is anomalous; that is, to determine if $s \notin \mathbb{S}^{(b)}$.

3.2 Proposed Solution

To leverage the advantageous properties of the SCDT, we first map the spectral signals to the SCDT domain and subsequently conduct anomaly detection in the transform space. In the transform domain, the background model defined in eq. (5) is expressed as:

$$\widehat{\mathbb{S}}^{(b)} = \bigcup_{m=1}^{M} \widehat{\mathbb{S}}_{\varphi_m^{(b)},\mathcal{G}}, \text{ with } \widehat{\mathbb{S}}_{\varphi_m^{(b)},\mathcal{G}} = \left\{\widehat{s}_{j,m}^{(b)} | \widehat{s}_{j,m}^{(b)} = g_j^{-1} \circ \widehat{\varphi}_m^{(b)}, g_j^{-1} \in \mathcal{G}^{-1}\right\}, \tag{6}$$

where $g_j^{-1} \circ \widehat{\varphi}_m^{(b)}$ denotes the SCDT of the signal $g_j' \varphi_m^{(b)} \circ g_j$, obtained using the composition property of the SCDT. The set $\mathcal{G}^{-1}$, defined in eq. (5), is convex by construction. Previous studies Rubaiyat et al. [2024a,b] have demonstrated that many practical signal classes can be modeled through such differentiable, strictly increasing deformations. Consequently, by the convexity property of the SCDT, each subset $\widehat{\mathbb{S}}_{\varphi_m^{(b)},\mathcal{G}}$ is convex for any template $\varphi_m^{(b)}$. Given, the set $\widehat{\mathbb{S}}^{(b)}$ is constructed as a union of subsets $\widehat{\mathbb{S}}_{\varphi_m^{(b)},\mathcal{G}}$, the background pixels can accordingly be viewed as lying in a union of multiple subspaces, with each subspace associated with one of these subsets. We therefore define the subspace generated by the convex set $\widehat{\mathbb{S}}_{\varphi_m^{(b)},\mathcal{G}}$ as:

$$\widehat{\mathbb{V}}_m^{(b)} = \text{span}\left(\widehat{\mathbb{S}}_{\varphi_m^{(b)},\mathcal{G}}\right). \tag{7}$$

By applying the definition of $\mathcal{G}^{-1}$ to eq. (6), the set $\mathbb{S}_{\varphi_m^{(b)},\mathcal{G}}$ in the SCDT domain can be expressed as

$$\widehat{\mathbb{S}}_{\varphi_m^{(b)},\mathcal{G}} = \left\{\left(\sum_{i=1}^{k} \alpha_i f_i\right) \circ \widehat{\varphi}_m^{(b)}, \alpha_i \geq 0\right\},$$

where $\{f_1, f_2, \ldots, f_k\}$ is a set of k linearly independent, strictly increasing functions, for example, integrals of positive basis functions such as Gaussian or polynomial functions. This formulation implies that the subspace $\widehat{\mathbb{V}}_m^{(b)}$ is k-dimensional.

Now, if a test data point $s \in \mathbf{S}$, belongs to the background, then it is generated according to the model in eq. (5). In such a scenario, there exists a template $\varphi_m^{(b)}$ such that $d^2(\widehat{s}, \widehat{\mathbb{V}}_m^{(b)}) = 0$, where, $d(\cdot,\cdot)$ denotes the Euclidean distance between $\widehat{s}$ and its nearest point in $\widehat{\mathbb{V}}_m^{(b)}$. Conversely if s is anomalous, it does not conform to the background model, and for every template $\varphi_m^{(b)}$, we have $d^2(\widehat{s}, \widehat{\mathbb{V}}_m^{(b)}) > 0$. Therefore, assuming that the background pixels in $\mathbf{S}$ are generated according to the model in eq. (5), the anomaly score for a test data point $s \in \mathbf{S}$ is defined as:

$$\varepsilon_a = \min_m \;\; d^2(\widehat{s}, \widehat{\mathbb{V}}_m^{(b)}), \;\; m = 1, 2, ..., M. \tag{8}$$

Since an anomalous point does not belong to any of the subspaces, the anomaly score ε_a will be higher for anomalous data points than for background pixels. It is worth noting that, although the model assumes background signals are generated from a set of templates $\varphi_m^{(b)}$ under deformations in $\mathcal{G}$, the algorithm does not require prior knowledge of either the templates or the deformation set.

Algorithm 1 Bootstrap sampling-based subspace modeling in SCDT domain for HAD

Input: HSI $\mathbf{S} = \{s_i\}_{i=1}^{N}$, parameters: number of bootstrap iterations N_e, number of pixels per iteration N_s
Output: Anomaly score ϵ_a for test signal $s \in \mathbf{S}$
for $l = 1$ to N_e **do**
    Draw N_s pixels from $\mathbf{S}$ with replacement to form $\mathbf{S}_l = \{s_i\}_{i=1}^{N_s} \subset \mathbf{S}$
    Compute SCDT of each sample in $\mathbf{S}_l$ and form: $\widehat{\mathbf{S}}_l = \{\widehat{s}_i\}_{i=1}^{N_s}$
    Apply PCA to $\widehat{\mathbf{S}}_l$ and choose k principal components explaining at least 99.99% of total variance
    Form subspace basis matrix $B_l = [b_1, b_2, \ldots, b_k]$ using the k components
end for
Compute anomaly score for test signal s:

$$\epsilon_a = \min_l \left\| \widehat{s} - B_l B_l^T \widehat{s} \right\|_{L_2}^2$$

3.3 Approximating Background Subspaces for Anomaly Detection

The proposed method begins by applying the SCDT to the spectral signals of a given HSI. Since all the datasets considered in this work contain non-negative spectral signals, we use the SCDT formulation in eq. (2) for all signals. The next step is to construct the subspace $\widehat{\mathbb{V}}_m^{(b)}$ in the SCDT domain. However, because the templates $\varphi_m^{(b)}$ are unknown and the problem is unsupervised, the subsets $\mathbb{S}_{\varphi_m^{(b)},\mathcal{G}}$ cannot be explicitly constructed. Consequently, it is not possible to directly estimate $\widehat{\mathbb{V}}_m^{(b)}$ using eq. (7). In this work, we adopt a bootstrap sampling strategy to construct multiple subsets of hyperspectral pixels from a given HSI. Specifically, we randomly draw N_s pixels ($N_s << N$) from the HSI $\mathbf{S}$ to form the first subset. This process is repeated N_e times with replacement, yielding a total of N_e subsets. Each subset is denoted as $\mathbf{S}_l = \{s_i\}_{i=1}^{N_s} \subset \mathbf{S}$, where $l = 1, 2, ..., N_e$. For each subset, we first apply the SCDT to every spectral signal in $\mathbf{S}_l$, yielding the transformed set $\widehat{\mathbf{S}}_l$. Next, PCA is performed on $\widehat{\mathbf{S}}_l$ and the k most significant principal components are extracted. Following Rubaiyat et al. [2025], the value of the parameter k is chosen such that the first k components explain at least 99.99% of the total variance of the HSI.

Let $B_l = [b_1, b_2, ..., b_k]$ denote the matrix whose columns are the k principal components of $\widehat{\mathbf{S}}_l$. Since each subset $\mathbf{S}_l$ is generated from randomly sampled pixels of an HSI that contains a large proportion of background pixels, the basis vectors in B_l predominantly span a background subspace. We denote this subspace as $\widetilde{\widehat{\mathbb{V}}}_l^{(b)}$, where $l = 1, 2, ..., N_e$. Although a bootstrap-generated subset $\mathbf{S}_l$ does not strictly satisfy the definition of $\mathbb{S}_{\varphi_m^{(b)},\mathcal{G}}$, in this work we assume that $\widetilde{\widehat{\mathbb{V}}}_l^{(b)}$ serves as an approximation to $\widehat{\mathbb{V}}_m^{(b)}$ for some pair of indices l and m. Under this assumption, the anomaly score in eq. (8) can be approximated as:

$$\varepsilon_a \approx \min_l \;\; d^2(\widehat{s}, \widetilde{\widehat{\mathbb{V}}}_l^{(b)}), \;\; l = 1, 2, ..., N_e. \tag{9}$$

For a test signal s, the corresponding anomaly score is computed by:

$$\varepsilon_a \approx \min_l \;\; \|\widehat{s} - B_l B_l^T \widehat{s}\|_{L_2}^2, \tag{10}$$

where $B_l B_l^T \widehat{s}$ represents the projection of $\widehat{s}$ onto the subspace spanned by the columns of B_l. Equivalently, this can be viewed as reconstructing $\widehat{s}$ using only the components within the background-dominated subspace $\widetilde{\widehat{\mathbb{V}}}_l^{(b)}$. Thus, if s is anomalous, its reconstruction error—and hence the anomaly score—will be larger than that of a background signal. Algorithm 1 outlines the proposed approach used to evaluate the anomaly score. Note that for a given set $\mathbf{S}_l$, the distance in eq. (10) is obtained in closed form, making the proposed method highly computationally efficient.

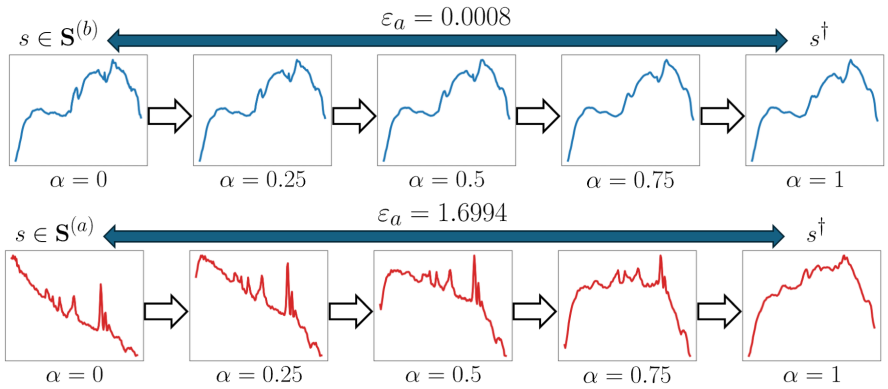

Figure 1: Visualizing the geodesic path p_α between a test datum and its projection onto the nearest subspace modeled by the proposed method. (Upper panel) Path between a background signal and its projection. Given the constructed subspace is background-dominated, both the projection and intermediate signals (for $\alpha = 0.25, 0.5, 0.75$) closely resemble the background signal $s \in \mathbf{S}^{(b)}$. (Lower panel) Path between an anomalous signal $s \in \mathbf{S}^{(a)}$ and its projection. In this case, the projection and path signals differ visibly from the original signal. Also note that the anomaly score ε_a is much smaller for the background signal than for the anomalous signal.

3.4 Geometric Interpretation of the Proposed Method

This section provides a preliminary interpretation of the proposed subspace modeling–based HAD method using the geometric properties of the SCDT embedding. According to Li et al. [2022], a geodesic does not necessarily exist between arbitrary signals in the SCDT space. However, a Euclidean geodesic exists between two signals s and $p := g's \circ g$ in the SCDT space, where $g : \mathbb{R} \to \mathbb{R}$ is a strictly increasing differentiable function. Given the SCDTs $\widehat{s}$ and $\widehat{p}$, as defined in eq. (2) for non-negative signals, the geodesic $\alpha \to p_\alpha, \forall \alpha \in [0, 1]$ is expressed as:

$$\widehat{p}_\alpha = \left[(1-\alpha)\|s\|_{L_1} + \alpha\|p\|_{L_1}\right]\left((1-\alpha)s^* + \alpha p^*\right) \tag{11}$$

in the SCDT domain. Here, $\widehat{p}_\alpha$ represents the SCDT of p_α, a point along the geodesic path. As outlined in the previous section, the proposed algorithm employs a bootstrap sampling approach to construct multiple subspaces representing the background spectral signals. The anomaly score for a test datum s is then computed as its distance to the nearest subspace in the SCDT domain. If the approach can accurately capture the subspace containing s, its projection $s^\dagger$ onto the corresponding subspace should ideally coincide with s; in practice, we observe $s^\dagger \approx s$. Moreover, the path defined by eq. (11) between s and $s^\dagger$ is expected to contain signals of similar shape (upper panel of Fig. 1). In contrast, for an anomalous signal $s \in \mathbf{S}^{(a)}$ that does not satisfy the model in eq. (5), the path may include signals of arbitrary shape (lower panel of Fig. 1).

4 Experiments and Results

Six hyperspectral datasets are used to evaluate the proposed method. AVIRIS-I Xu et al. [2015], collected over San Diego, CA, USA using the Airborne Visible/Infrared Imaging Spectrometer (AVIRIS), contains 224 spectral bands, of which 186 bands are retained after removing low-SNR bands. A 100×100 subregion is selected from the upper-left corner of the full AVIRIS scenario, with airplane pixels labeled as anomalies. AVIRIS-II Huyan et al. [2018], a 200×200 subregion from the same AVIRIS image, includes more diverse background materials, and airplane pixels are again considered anomalous. The HYDICE Urban dataset Xu et al. [2015] has a spatial size of 307×307 pixels with 162 bands. It depicts an urban scene with vegetation, construction sites, and roads, where roof pixels are marked as anomalous. The Pavia University dataset Grana et al. [2021], acquired by the ROSIS (Reflective Optics System Imaging Spectrometer) sensor, contains 610×340 pixels and 103 spectral bands. It provides an aerial view of a campus area with various land-cover types, where painted metal sheets are treated as anomalies. The Airport dataset Kang et al. [2017], collected over Gulfport city by the AVIRIS sensor, consists of 100×100 pixels and 191 bands, and contains three anomalous aircraft of different sizes and shapes. Finally, the HYDICE Forest Radiance I dataset

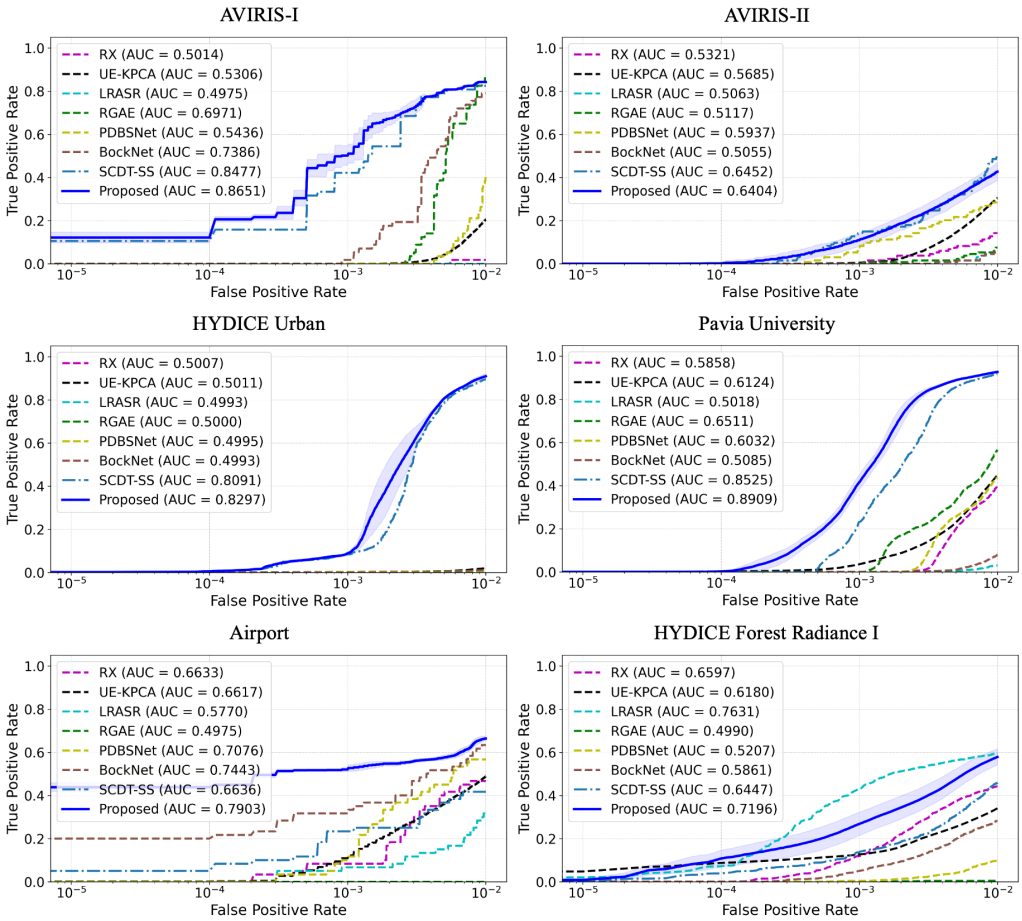

Figure 2: ROC curves and AUC scores ($FPR \leq 10^{-2}$) for all methods across six hyperspectral datasets. The dark blue curve represents the average ROC of the proposed method over 50 runs, with the shaded area indicating one standard deviation (computed using Python NumPy; TPR values assumed normally distributed at each FPR value). Results are reported up to $FPR \leq 10^{-2}$ to emphasize performance under low FPRs. Experiments for the proposed method were run on Windows 10 with a 13th Gen Intel Core i9-13950HX CPU and 64 GB RAM. The associated run times averaged across the 50 runs were approximately 28, 89, 328, 231, 37, and 282 seconds for the Aviris I, Aviris II, Urban, Pavia, Airport, and Forest datasets, respectively.

Olsen et al. [1997] consists of 210 spectral bands, of which 158 are retained. Following Olson and Doster [2017], a 600×293 subregion from the original 1280×308 image is used for evaluation.

To benchmark the proposed approach, we compared its performance with several widely used anomaly detection techniques, including Reed–Xiaoli (RX) Reed and Yu [1990], unsupervised ensemble-kernel PCA (UE-KPCA) Merrill and Olson [2020], low-rank and sparse representation (LRASR) Xu et al. [2015], robust graph autoencoders (RGAE) Fan et al. [2021], pixel-shuffle downsampling blind-spot reconstruction network (PDBSNet) Wang et al. [2023b], and blind-block reconstruction network (BockNet) Wang et al. [2023a]. Additionally, to highlight the improvement over single subspace modeling, we included a comparison with the SCDT-SS method proposed in Rubaiyat et al. [2025]. To implement the proposed method, we utilized the SCDT functionality from the PyTransKit package Imaging and data science lab [2021] and the PCA module from scikit-learn Pedregosa et al. [2011]. The parameters N_s and N_e were empirically set to 256 and 128, respectively; future work may investigate systematic approaches for their optimization. The evaluation was carried out on the six hyperspectral datasets introduced above. Performance was measured using the area under the receiver operating characteristic (ROC) curve (AUC), which is a widely adopted metric in anomaly detection. The AUC ranges from 0 to 1, with higher values corresponding to stronger discrimination between anomalous and background pixels.

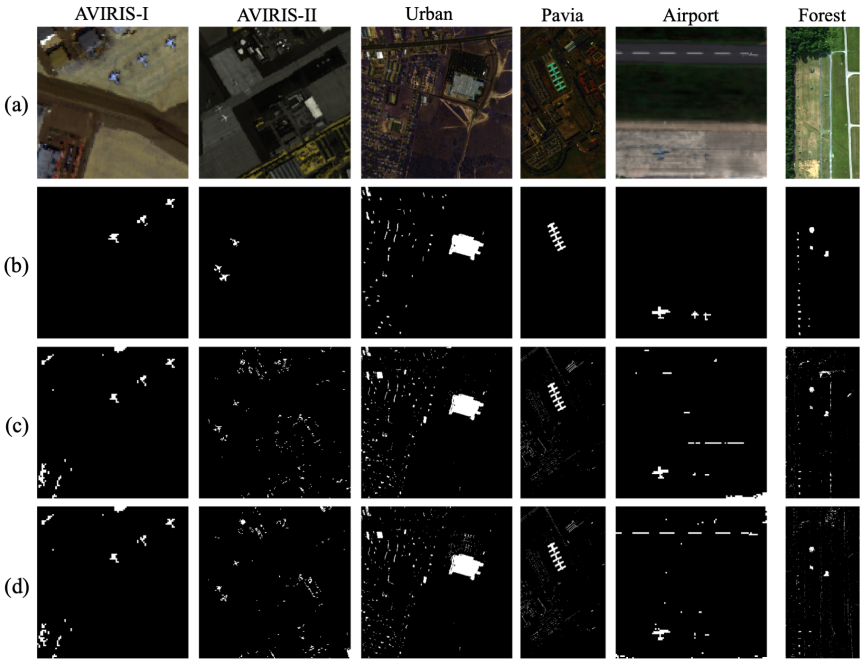

Figure 3: Row (a): Approximate RGB images of the datasets; (b) corresponding ground-truth maps; (c) binary detection maps generated by the proposed method with a specific threshold for each set that yields $FPR = 10^{-2}$; and (d) binary detection maps generated by the best competing methods with thresholds corresponding to $FPR = 10^{-2}$. From left to right, the best competing methods are SCDT-SS for AVIRIS-I, AVIRIS-II, Urban, and Pavia, and BockNet and LRASR for Airport and Forest, respectively.

The AUC score is generally obtained by integrating the ROC curve up to a false positive rate (FPR) of 10^0. In practice, however, detection performance at low FPR values is often more critical. Fig. 2 presents the ROC curves and AUC scores up to $FPR = 10^{-2}$ for all comparative methods across the six datasets. Due to the stochastic nature of the bootstrap sampling strategy, the proposed method was executed 50 times per dataset. The dark blue curve in Fig. 2 represents the average ROC, with the shaded region indicating one standard deviation. The results indicate that the proposed method outperforms other approaches on four datasets—AVIRIS-I, HYDICE Urban, Pavia University, and Airport. For AVIRIS-II, the method achieves nearly the same performance as SCDT-SS, the best-performing competing method, implying that the dataset's background is effectively captured by a single subspace in the SCDT domain. On the HYDICE Forest Radiance I dataset, however, the proposed method attains a slightly lower AUC under FPR $\leq 10^{-2}$ compared to LRASR.

Fig. 3 illustrates the binary detection maps obtained with thresholds chosen to maintain an FPR of 10^{-2} for each dataset. The approximate RGB images of the HSI datasets are provided in Fig. 3(a), and the corresponding ground-truth anomaly maps are shown in Fig. 3(b). The detection maps generated by the proposed method appear in row (c), while those from the best-performing competing methods are shown in Fig. 3(d). Overall, the proposed method achieves more precise anomaly localization with fewer false alarms across most datasets. Notably, on HYDICE Urban and Airport, it provides substantial improvements over competing approaches, underscoring the benefit of modeling multiple background subspaces. For AVIRIS-I, AVIRIS-II, and Pavia University, the detection maps are nearly indistinguishable from those of SCDT-SS, which aligns with the quantitative results discussed earlier. This demonstrates that the proposed extension of the SCDT-SS framework is able to consistently improve upon the single-subspace model, or at the very least, match its performance when the latter already provides an adequate representation. The only case of relatively weaker performance is observed on Forest Radiance I, where tree shadows combined with a small road segment create considerable background variability, causing some regions to be misclassified as anomalous and resulting in slightly lower performance compared to LRASR. These qualitative findings not only support the quantitative evidence in Fig. 2 but also highlight the robustness of the proposed approach

across diverse hyperspectral scenes. Taken together, the results demonstrate the practical effectiveness of the method and motivate its application to real-world anomaly detection tasks.

5 Conclusion

We describe a novel transport-based multiple subspace modeling approach for hyperspectral anomaly detection where the problem is formulated under the assumption that the spectral signals of background pixels are observations of a set of arbitrary templates subjected to strictly increasing deformations of a specific form. We then introduce a bootstrap sampling strategy in the ambient domain and construct multiple subspaces in the SCDT domain that characterize the background space of a hyperspectral image. The anomaly score for each test signal is then computed as its distance to the nearest subspace in the SCDT domain. By modeling multiple subspaces to capture varied background spectral characteristics, the proposed method robustly identifies anomalous pixels across diverse and challenging hyperspectral scenes characterized by varied background spectral classes. Experimental results on six datasets demonstrate that the approach consistently achieves accurate and robust detection, often outperforming or closely matching the performance of existing techniques. Moreover, due to the geodesic property of the SCDT embedding, the method is inherently interpretable, as its operations and decisions can be understood in terms of geometric relationships within the transform domain. These findings highlight the method's ability to handle diverse hyperspectral scenes, underscoring its potential as a practical and reliable tool for real-world hyperspectral anomaly detection. Future work will focus on gaining a deeper understanding of the bootstrap-based approximation of background subspaces and developing systematic strategies for selecting optimal values of the parameters N_s and N_e. We also plan to investigate more cluttered hyperspectral scenarios to better characterize when multiple background subspaces offer advantages over a single-subspace model.

Acknowledgments and Disclosure of Funding

This work was supported by the Office of Naval Research (ONR).

References

Akram Aldroubi, Rocio Diaz Martin, Ivan Medri, Gustavo K Rohde, and Sumati Thareja. The signed cumulative distribution transform for 1-d signal analysis and classification. *Foundations of Data Science*, 4(1):137–163, 2022.

Tegan H Emerson, Timothy Doster, and Colin C Olson. Path-based background model augmentation for hyperspectral anomaly detection. In *2018 9th Workshop on Hyperspectral Image and Signal Processing: Evolution in Remote Sensing (WHISPERS)*, pages 1–5. IEEE, 2018.

G. Fan, Y. Ma, X. Mei, F. Fan, J. Huang, and J. Ma. Hyperspectral anomaly detection with robust graph autoencoders. *IEEE Transactions on Geoscience and Remote Sensing*, pages 1–14, 2021.

Pradeep K Goel, Shiv O Prasher, Ramanbhai M Patel, Jacques-André Landry, RB Bonnell, and Alain A Viau. Classification of hyperspectral data by decision trees and artificial neural networks to identify weed stress and nitrogen status of corn. *Computers and Electronics in Agriculture*, 39 (2):67–93, 2003.

M Grana, MA Veganzons, and B Ayerdi. Hyperspectral remote sensing scenes–grupo de inteligencia computacional (gic). *URL https://www. ehu. eus/ccwintco/index. php/Hyperspectral_Remote_ Sensing_Scenes*, 2021.

Ning Huyan, Xiangrong Zhang, Huiyu Zhou, and Licheng Jiao. Hyperspectral anomaly detection via background and potential anomaly dictionaries construction. *IEEE Transactions on Geoscience and Remote Sensing*, 57(4):2263–2276, 2018.

Imaging and data science lab. PyTransKit. `https://github.com/rohdelab/PyTransKit`, 2021.

Xudong Kang, Xiangping Zhang, Shutao Li, Kenli Li, Jun Li, and Jón Atli Benediktsson. Hyperspectral anomaly detection with attribute and edge-preserving filters. *IEEE Transactions on Geoscience and Remote Sensing*, 55(10):5600–5611, 2017.

Heesung Kwon and Nasser M Nasrabadi. Kernel RX-algorithm: A nonlinear anomaly detector for hyperspectral imagery. *IEEE transactions on Geoscience and Remote Sensing*, 43(2):388–397, 2005.

Chenyu Li, Bing Zhang, Danfeng Hong, Jing Yao, and Jocelyn Chanussot. Lrr-net: An interpretable deep unfolding network for hyperspectral anomaly detection. *IEEE Transactions on Geoscience and Remote Sensing*, 61:1–12, 2023.

Shiying Li, Abu Hasnat, Mohammad Rubaiyat, and Gustavo K Rohde. Geodesic properties of a generalized wasserstein embedding for time series aanalysis. In *Topological, Algebraic and Geometric Learning Workshops 2022*, pages 216–225. PMLR, 2022.

Guangcan Liu, Zhouchen Lin, Shuicheng Yan, Ju Sun, Yong Yu, and Yi Ma. Robust recovery of subspace structures by low-rank representation. *IEEE transactions on pattern analysis and machine intelligence*, 35(1):171–184, 2012.

Stefania Matteoli, Marco Diani, and Giovanni Corsini. Improved estimation of local background covariance matrix for anomaly detection in hyperspectral images. *Optical Engineering*, 49(4): 046201–046201, 2010.

Nicholas Merrill and Colin C Olson. Unsupervised ensemble-kernel principal component analysis for hyperspectral anomaly detection. In *Proceedings of the IEEE/CVF conference on computer vision and pattern recognition workshops*, pages 112–113, 2020.

Nasser M Nasrabadi. Regularization for spectral matched filter and RX anomaly detector. In *Algorithms and Technologies for Multispectral, Hyperspectral, and Ultraspectral Imagery XIV*, volume 6966, pages 28–39. SPIE, 2008.

Richard Chris Olsen, Steve Bergman, and Ronald G Resmini. Target detection in a forest environment using spectral imagery. In *Imaging Spectrometry III*, volume 3118, pages 46–56. SPIE, 1997.

Colin C Olson and Timothy Doster. A novel detection paradigm and its comparison to statistical and kernel-based anomaly detection algorithms for hyperspectral imagery. In *Proceedings of the IEEE Conference on Computer Vision and Pattern Recognition Workshops*, pages 108–114, 2017.

Se Rim Park, Soheil Kolouri, Shinjini Kundu, and Gustavo K Rohde. The cumulative distribution transform and linear pattern classification. *Applied and computational harmonic analysis*, 45(3): 616–641, 2018.

F. Pedregosa, G. Varoquaux, A. Gramfort, V. Michel, B. Thirion, O. Grisel, M. Blondel, P. Prettenhofer, R. Weiss, V. Dubourg, J. Vanderplas, A. Passos, D. Cournapeau, M. Brucher, M. Perrot, and E. Duchesnay. Scikit-learn: Machine learning in Python. *Journal of Machine Learning Research*, 12:2825–2830, 2011.

Irving S Reed and Xiaoli Yu. Adaptive multiple-band CFAR detection of an optical pattern with unknown spectral distribution. *IEEE transactions on acoustics, speech, and signal processing*, 38 (10):1760–1770, 1990.

Abu Hasnat Mohammad Rubaiyat, Mohammad Shifat-E-Rabbi, Yan Zhuang, Shiying Li, and Gustavo K Rohde. Nearest subspace search in the signed cumulative distribution transform space for 1d signal classification. In *ICASSP 2022-2022 IEEE International Conference on Acoustics, Speech and Signal Processing (ICASSP)*, pages 3508–3512. IEEE, 2022.

Abu Hasnat Mohammad Rubaiyat, Shiying Li, Xuwang Yin, Mohammad Shifat-E-Rabbi, Yan Zhuang, and Gustavo K Rohde. End-to-end signal classification in signed cumulative distribution transform space. *IEEE Transactions on Pattern Analysis and Machine Intelligence*, 2024a.

Abu Hasnat Mohammad Rubaiyat, Duy H Thai, Jonathan M Nichols, Meredith N Hutchinson, Samuel P Wallen, Christina J Naify, Nathan Geib, Michael R Haberman, and Gustavo K Rohde. Data-driven identification of parametric governing equations of dynamical systems using the signed cumulative distribution transform. *Computer Methods in Applied Mechanics and Engineering*, 422:116822, 2024b.

Abu Hasnat Mohammad Rubaiyat, Jordan Vincent, and Colin Olson. Improved hyperspectral anomaly detection via unsupervised subspace modeling in the signed cumulative distribution transform domain, 2025. URL `https://arxiv.org/abs/2510.00148`.

Hongjun Su, Zhaoyue Wu, Huihui Zhang, and Qian Du. Hyperspectral anomaly detection: A survey. *IEEE Geoscience and Remote Sensing Magazine*, 10(1):64–90, 2021.

Kun Tan, Fuyu Wu, Qian Du, Peijun Du, and Yu Chen. A parallel gaussian–bernoulli restricted boltzmann machine for mining area classification with hyperspectral imagery. *IEEE Journal of Selected Topics in Applied Earth Observations and Remote Sensing*, 12(2):627–636, 2019.

Sumati Thareja, Gustavo Rohde, Rocio Diaz Martin, Ivan Medri, and Akram Aldroubi. Signed cumulative distribution transform for parameter estimation of 1-d signals. *arXiv preprint arXiv:2207.07989*, 2022.

Degang Wang, Lina Zhuang, Lianru Gao, Xu Sun, Min Huang, and Antonio Plaza. BockNet: Blind-block reconstruction network with a guard window for hyperspectral anomaly detection. *IEEE Trans. Geosci. Remote Sens.*, 61:1–16, 2023a. doi: 10.1109/TGRS.2023.3335484.

Degang Wang, Lina Zhuang, Lianru Gao, Xu Sun, Min Huang, and Antonio Plaza. PDBSNet: Pixel-shuffle downsampling blind-spot reconstruction network for hyperspectral anomaly detection. *IEEE Trans. Geosci. Remote Sens.*, 61:1–14, 2023b. doi: 10.1109/TGRS.2023.3276175.

Min Xu, Hongxing Liu, Richard Beck, John Lekki, Bo Yang, Song Shu, Yang Liu, Teresa Benko, Robert Anderson, Roger Tokars, et al. Regionally and locally adaptive models for retrieving chlorophyll-a concentration in inland waters from remotely sensed multispectral and hyperspectral imagery. *IEEE Transactions on Geoscience and Remote Sensing*, 57(7):4758–4774, 2019.

Yang Xu, Zebin Wu, Jun Li, Antonio Plaza, and Zhihui Wei. Anomaly detection in hyperspectral images based on low-rank and sparse representation. *IEEE Transactions on Geoscience and Remote Sensing*, 54(4):1990–2000, 2015.